The first measurement of the differential cross-sections for the electroweak production of
ZZ in association with two jets in the four-leptons final state in 13 TeV proton-proton
collision with the ATLAS detector.

A Dissertation

Presented to

The Faculty of the Graduate School of Arts and Sciences
Brandeis University

Department of Physics

Professor Gabriella Sciolla, Advisor

In Partial Fulfillment
of the Requirements for the Degree
Doctor of Philosophy

by
Prajita Bhattarai

May 2023

This dissertation, directed and approved by Prajita Bhattarai's Committee, has been accepted and approved by the Faculty of Brandeis University in partial fulfillment of the requirements for the degree of:

DOCTOR OF PHILOSOPHY

Wendy Cadge, Dean
Graduate School of Arts and Sciences

Dissertation Committee:
Professor Gabriella Sciolla, Department of Physics, Brandeis University
Professor Aram Apyan, Department of Physics, Brandeis University
Dr. Alessandro Tricoli, Brookhaven National Laboratory

ABSTRACT

The first measurement of the differential cross-sections for the electroweak production of ZZ in association with two jets in the four-leptons final state in 13 TeV proton-proton collision with the ATLAS detector.

A dissertation presented to the Faculty of the
Graduate School of Arts and Sciences of Brandeis University
Waltham, Massachusetts

By Prajita Bhattarai

Table of Contents

I Introduction   1

II Theory   2

III The Large Hadron Collider   27

VII Conclusion 47

VIII Outlook 48

References 49

Appendices 52

Appendices 52

List of Tables

List of Figures

- BSM: Beyond the Standard Model

- C: Charge conjugation

- EFT: Effective Field Theory

- EWK: Electroweak

- FSR: Final State Radiation

- GRL: Good Run List

- H: Weak Hypercharge

- I: Weak Isospin

- $\mathcal{L}_{\mathcal{SM}}$: Lagrangian

- LB: Luminosity Block

- LH: Left Handed

- MC: Monte Carlo

- P: Parity

- PDF: Parton Distribution Function

- Q: Electric Charge

- QGC: Quartic Gauge Coupling

- QED: Quantum Electrodynamics

- QCD: Quantum Chromodynamics

- $(\mathcal{P})$: Poincare group

- RH: RightHanded

- SF-OC: Same-flavor, Opposite-charged

- SM: Standard Model

- T: Time-reversal

- TGC: Triple Gauge Coupling

- TTVA: Track-to-vertex association

- VBS: Vector Boson Scattering

- VEV: Vacuum Expectation Value

Chapter I: Introduction

Chapter II: Theory

This chapter describes the theoretical framework of the experimental measurements discussed in this thesis. The Standard Model (SM) of particle physics is introduced, and concepts relevant to the thesis are discussed in Section 1. Section 2 discusses the outstanding problems with the Standard Model, thus, motivating the experimental measurement. Section 3 discusses the phenomenology of the proton-proton collisions relevant to this thesis whereas, Section 4 discusses the physics of two Z bosons production in association of two jets.

1 The Standard Model

The SM of particle physics is a mathematical framework based on quantum field theory which incorporates quantum mechanics and special relativity. The SM describes all known fundamental particles in nature and their interactions. It consists of two sets of particles with intrinsic angular momentum, half-integer-spin fermions that are fundamental constituents of matter particles, and force-carrying integer-spin bosons. The seventeen fundamental particles of the SM and their properties such as mass, charge, and intrinsic spin are shown schematically by figure 1. Discussion in this section is written with the guidance from two textbooks on particle physics, Mark Thomson's Modern Particle Physics [7], and Halzen & Martin's Quarks & Leptons [2].

1.1 Symmetries

The fundamental particles of the SM and their interactions can be described by constructing a general renormalizable Lagrangian ($\mathcal{L}_{SM}$) that respects certain sets of given symmetries. The Lagrangian of the SM is independent of the reference frame, naturally respecting the complete external symmetries of special relativity, the Poincare group ($\mathcal{P}$). Thus, the SM is invariant under spacetime translations, boosts, and rotations. Additionally, by the construction of the Lagrangian, the SM respects an internal local gauge symmetry $SU(3)_C \otimes SU(2)_L \otimes U(1)_Y$. The $SU(3)_C$ symmetry is associated with the Quantum Chromodynamics (QCD) discussed in detail in Section 1.3.3. The $SU(2)_L \otimes U(1)_Y$ gauge symmetry discussed in 1.3.4 is associated with the unified electroweak theory that combines Quantum Electrodynamics (QED) and the weak interactions.

According to Noether's theorem, a quantity is conserved for each continuous transformation that leaves the Lagrangian invariant [8]. Several interesting physical quantum numbers are conserved as a consequence of the symmetries respected by the SM. The $SU(3)_C$ in QCD conserves color charge. Weak isospin (I) and weak hypercharge (Y) are the quantum

numbers associated with the $SU(2)_L$ and $U(1)_Y$ gauge groups respectively. At low energies the $SU(2)_L \otimes U(1)_Y$ symmetry is spontaneously broken and will be discussed in Section 1.3.4. The $SU(2)_L$ group follows a chiral structure where the gauge fields couple explicitly to the left-handed (LH) chiral fermions states and the right-handed (RH) chiral anti-fermions states.

The SM also respects CPT symmetry, a combination of three additional discrete symmetries, charge conjugation (C), parity (P), and time-reversal (T). The charge-conjugation transformation transforms particles to anti-particles by reversing the quantum numbers, whereas, the parity transformation transforms left-handed particles to right-handed particles.

1.2   Particles and Fields
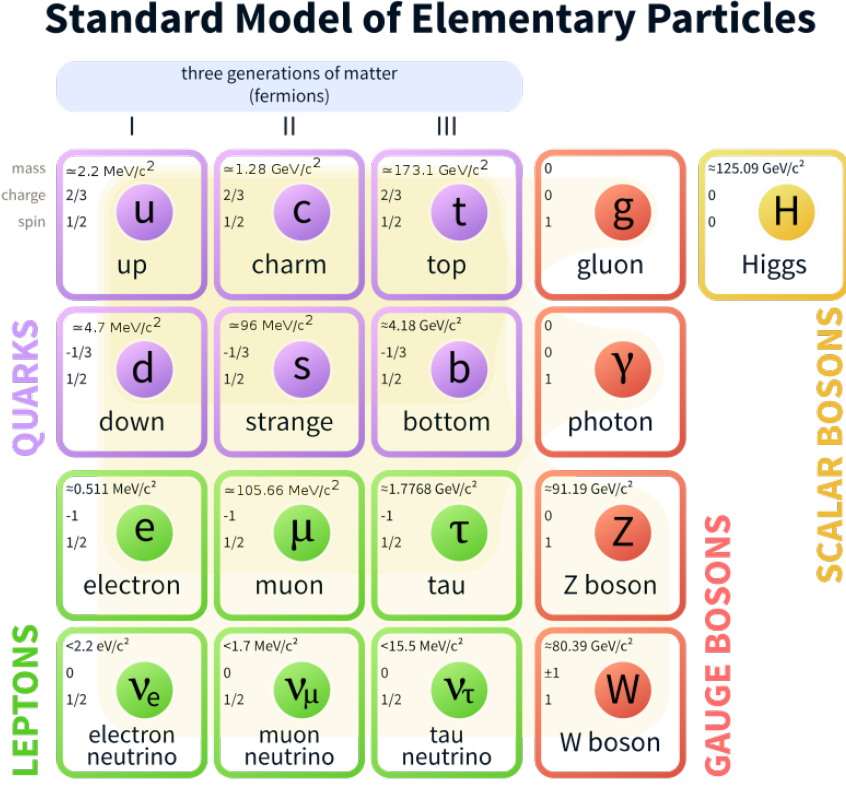
Figure 1: The seventeen fundamental particles of the SM include three generations of twelve fermions, four gauge bosons, and the scalar Higgs bosons. [3]

The twelve half-integer-spin fermions can be distinguished further into two categories, leptons, and quarks, each having three generations of particles with similar properties as shown schematically by figure 1. For each fermion, there exists an anti-fermion with the same additive quantum numbers but with opposite signs. Four spin 1 bosons shown in Table 1 are collectively called the gauge bosons. Quanta of these gauge fields mediate the electromagnetic, weak, and strong interactions and are invariant under various local gauge transformations [9]. As summarized by Table 2, fermions take part in different interactions. The strength of interaction is governed by a gauge coupling parameter.

Massless photon (γ) mediates the electromagnetic interaction. The massive W and Z

Table 1: Properties of SM gauge bosons. [1]

Interaction Type		Particle	Q	Mass $[GeV]$	Symmetry Group
Electroweak	Electromagnetic	Photon (γ)	0	0	$SU(2) \otimes U(1)$
	Weak	$W^{\pm}$	± 1	80.4	
		Z boson	0	91.2	
Strong		gluons (g)	0	0	$SU(3)$

Table 2: Summary of different interactions of fermions under different gauge theory. The check mark suggests that the fermions interact via associated force.

Particles		Strong $SU(3)$	Electromagnetic $U(1)$	Weak $SU(2)$
Quarks	u, c, t d, s, b	✓	✓	✓
Leptons	e, μ, τ	-	✓	✓
	ν_e, ν_μ, ν_τ	-	✓	-

bosons mediate weak interaction. The electric charge (Q) which is conserved in all interactions is related to the isospin and hypercharge by $Q = I_3 + \frac{Y}{2}$, where I_3 is the third component of the weak isospin. As a consequence of the chiral structure of $SU(2)_L$, each generation of fermion contains a left-handed doublet with $I_3 = \pm\frac{1}{2}$ and a right-handed singlet carrying $I_3 = 0$ which are shown in Table 3.

Each generation of lepton, electron (e), muon (μ) and tau (τ) is accompanied by a neutral particle called neutrino (ν) with same lepton flavor $(\nu_e, \nu_\mu \& \nu_\tau)$. The SM neutrinos are their own anti-particles and only left-handed neutrinos are predicted by the theory. The lepton flavor is conserved by the SM in all interactions.

The quarks can be further categorized into two categories, the up-type quarks with $+\frac{2}{3}$ charge and the down-type quarks with $-\frac{1}{3}$ charge. Up (u), charm (c), & top (t) are the first, second, and third generation of the up-type quarks, while the down (d), strange (s) & bottom (b) are the three generations of the down-type quarks. The down-type left-handed quarks in $SU(2)_L$ quark doublets d', s' & b' summarized in table 3 are linear combinations of d, s, b quarks. The quarks interact strongly with one another by strong interaction mediated by

Table 3: Electroweak quantum numbers of the SM half-integer spin fermions (quarks and leptons) arranged in a left-handed $SU(2)$ doublet and right-handed $SU(2)$ singlet. [2]

Particle Types	First	Second	Third	I_3	Y	Q
Leptons	$\begin{pmatrix} e \\ \nu_e \end{pmatrix}_L$	$\begin{pmatrix} \mu \\ \nu_\mu \end{pmatrix}_L$	$\begin{pmatrix} \tau \\ \nu_\tau \end{pmatrix}_L$	$-\frac{1}{2}$ $\frac{1}{2}$	-1 -1	-1 0
	e_R	μ_R	τ_R	0	-2	-1
Quarks	$\begin{pmatrix} u \\ d' \end{pmatrix}_L$	$\begin{pmatrix} c \\ s' \end{pmatrix}_L$	$\begin{pmatrix} t \\ b' \end{pmatrix}_L$	$\frac{1}{2}$ $-\frac{1}{2}$	$\frac{1}{3}$ $\frac{1}{3}$	$\frac{2}{3}$ $-\frac{1}{3}$
	u_R	c_R	t_R	0	$\frac{4}{3}$	$\frac{2}{3}$
	d_R	s_R	b_R	0	$-\frac{2}{3}$	$-\frac{1}{3}$

the massless neutral gluons which follow from $SU(3)$ gauge symmetry by exchange of color charges. Each quark can have either one of the three color charges (red, blue &, green), whereas an anti-quark can have either an anti-red, anti-blue or anti-green color charge. There are eight gluons in the SM with color charges formed by a combination of either of the two color charges. Since gluons have a color charge, they interact with other gluons strongly. Only color neutral hadronic states formed by a combination of quarks and gluons are observed experimentally.

Higgs boson is the only spin-0 scalar particle in the theory with no charge and gives masses to all other particles through Spontaneous Symmetry Breaking which will be discussed in Section 1.3.4.

1.3   Theoretical Formulation of the Standard Model

Relativistic quantum field theory is the theoretical framework of the SM that describes elementary particles and their interactions. This section introduces the framework.

1.3.1 Lagrangian of the Standard Model

The dynamics of the SM can be described by the Lagrangian density given in equation 1.1 which is invariant under the local gauge transformation of the $SU(3) \otimes SU(2)_L \otimes U(1)_Y$ symmetry group.

$$\mathcal{L}_{SM} = -\frac{1}{4}F_{\mu\nu}F^{\mu\nu} \; + \; i\bar{\psi}\gamma^{\mu}D_{\mu}\psi \; + \; |D_{\mu}\phi|^2 \; + \; -V(\phi) + \bar{\psi}_i y_{ij}\psi_j\phi \; + \; h.c. \tag{1.1}$$

The first term $-\frac{1}{4}F_{\mu\nu}F^{\mu\nu}$ describes the dynamics of the gauge boson interactions, the second term $i\bar{\psi}\gamma^{\mu}D_{\mu}\psi$ describes the interaction of the fermion fields. The third term $|D_{\mu}\phi|^2$ describes the couplings between the Higgs boson and gauge bosons, whereas the term $V(\phi)$ describes the Higgs potential and its self-interactions. The second last term $\bar{\psi}_i y_{ij}\psi_j\phi$ generates masses for fermions based on their Yukawa couplings y_{ij} to the Higgs field. Similarly, the last term $h.c.$ generates masses for antifermions.

1.3.2 Quantum Electrodynamics

Quantum electrodynamics describes electromagnetic interaction. The Lagrangian density ($\mathcal{L}_{Dirac}$) describes the free propagation of a fermion in a vacuum as:

$$\mathcal{L}_{Dirac} = \bar{\psi}i\gamma^{\mu}\partial_{\mu}\psi \; - \; m\bar{\psi}\psi \tag{1.2}$$

,

where ψ is the fermionic spinor, γ^{μ} represents the Dirac matrices with μ being the Lorentz index running from 0 to 3, ∂^{μ} is the covariant derivative and m is the mass of the fermion.

The Lagrangian in equation 1.2 is invariant under a $U(1)$ global gauge transformation,

$$\psi \rightarrow \psi^{'} = e^{iq\alpha}\psi, \tag{1.3}$$

where q is a parameter of the transformation itself and α is a real phase factor. However,

under the local gauge transformation of form

$$\psi \rightarrow \psi^{'} = e^{iq\alpha(x)}\psi \tag{1.4}$$

which α depends on $x = (x_0, x_1, x_2, t)$ the Dirac Lagrangian in equation 1.2 is not invariant.

To make the Lagrangian of equation 1.2 invariant, a gauge field A_μ is introduces with the following transformation properties,

$$A_\mu \rightarrow A_\mu - \partial_\mu \alpha \tag{1.5}$$

The A_μ couples to fermionic fields $\psi(x, t)$ with strength q. A covariant derivative specific to the local gauge transformation is defined as:

$$D_\mu = \partial_\mu - iqA_\mu \tag{1.6}$$

The quantity q can be interpreted as the electric charge $-e$ of fermion which gives the coupling strength of QED. With these substitutions, the Dirac Lagrangian in equation 1.2 changes to following

$$\mathcal{L} = \bar{\psi}(i\gamma^\mu D_\mu - m)\psi \tag{1.7}$$

,

which is invariant under $U(1)$ gauge transformation respecting the $U(1)$ gauge symmetry.

The gauge field A_μ can be interpreted as the photon field and is related to the electromagnetic field tensor by

$$F_{\mu\nu} = \partial_\mu A_\nu - \partial_\nu A_\mu \tag{1.8}$$

The gauge invariant kinetic term of photon $-\frac{1}{4}F_{\mu\nu}F^{\mu\nu}$ can be inserted into the Lagrangian

in equation 1.7 which gives us the full Lagrangian of QED invariant under $U(1)$ gauge transformation.

$$\mathcal{L}_{QED} = -\frac{1}{4}F_{\mu\nu}F^{\mu\nu} + \bar{\psi}(i\gamma^\mu D_\mu - m)\psi \tag{1.9}$$

$\mathcal{L}_{QED}$ in equation 1.9 is the full Lagrangian for QED and the electromagnetic phenomena can be derived by solving for the equations of motion applying the Lorentz gauge condition $\partial_\mu A^\mu = 0$.

1.3.3 Quantum Chromodynamics

Interaction between the quarks is defined by Quantum Chromodynamics requiring $SU(3)$ gauge transformation on the quark field with color charge j (red, blue, or green).

The Dirac Lagrangian for a quark can be modified to include all possible colors of quark field q_j as

$$\mathcal{L} = \bar{q}_j(i\gamma^\mu\partial_\mu - m)q_j \tag{1.10}$$

The generators of the $SU(3)$ group are eight linearly independent traceless Gell-Mann matrices that do not commute with each other such that

$$[T_a, T_b] = if_{abc}T_c \tag{1.11}$$

where f_{abc} is the structure constant of $SU(3)$

The local $SU(3)$ gauge transformation is

$$q(x) \rightarrow e^{i\alpha_a(x)T_a}q(x) \tag{1.12}$$

where $T_a = \frac{\lambda_a}{2}$, and $a = 1, 2...8$. To understand the source of gauge invariance in the Lagrangian in equation , we can consider an infinitesimal transformation of the color field as

$$q(x) \rightarrow [1 + i\alpha_a(x)T_a]q(x) \ni \partial_\mu q \rightarrow (1 + i\alpha_a T_a)\partial_\mu q + iT_a q \partial_\mu \alpha_a \tag{1.13}$$

The last term $iT_a q \partial_\mu \alpha_a$ breaks the gauge invariance. Similar to QED, eight gauge fields corresponding to each $a = 1, 2...8$ G_μ^a with following transformation properties are introduced

$$G_\mu^a \rightarrow G_\mu^a - \frac{1}{g_s}\partial_\mu \alpha_a - f_{abc}\alpha_b G_\mu^c \tag{1.14}$$

These gauge fields G_μ^a are the gluon fields. Similar to QED the covariant derivative is defined as

$$D_\mu = \partial_\mu + ig_s \frac{\lambda_a}{2} G_\mu^a \tag{1.15}$$

where g_s is the coupling strength of the gluon fields to the quark fields.

The Lagrangian density in equation 1.10 is then

$$\mathcal{L} = \bar{q}_j(i\gamma^\mu D_\mu - m)q_j \tag{1.16}$$

Similar to QED, a gauge-invariant kinetic term $-\frac{1}{4}G_{\mu\nu}^a G_a^{\mu\nu}$,

dependent on the field strength tensor $G_{\mu\nu}^a$ is added to equation 1.16 to give the full QCD Lagrangian. The kinetic terms allow self-interaction within the gluon fields which is an important feature of QCD. $G_{\mu\nu}^a$ is the field strength tensor defined as

$$G_{\mu\nu}^a = \partial_\mu G_\nu^a - \partial_\nu G_\mu^a - g_s f_{abc} G_\mu^b G_\nu^c \tag{1.17}$$

Therefore, the complete $SU(3)$ gauge invariant Lagrangian describing the quarks and gluons interaction is

$$\mathcal{L}_{QCD} = \bar{q}_j(i\gamma^\mu D_\mu - m)q_j - \frac{1}{4}G_{\mu\nu}^a G_a^{\mu\nu} \tag{1.18}$$

1.3.4 Electroweak Theory

Weak interactions describe the interactions mediated by massive gauge bosons. The first formulation of the weak interaction was made by Fermi in 1934, to explain the beta decay using four fermion interaction vertex. The formulation successfully describes the beta decay at low energies when the interaction energy is much smaller than the W boson mass. A unified electroweak theory was formulated by Glashow in 1961 [10], by extending the $SU(2)$ symmetric non-Abelian gauge theory formulated by Yang and Mills in 1954 [11] to $SU(2) \otimes U(1)$ gauge theory. Above the unification threshold, the differences in the electromagnetic and weak interactions are not apparent.

Experimental observations suggest that weak interactions violate parity by only affecting the left-handed fermion fields and the right-handed anti-fermion fields. Thus the unified electroweak theory are described by $SU(2)_L \otimes U(1)_Y$ gauge interactions. Similar to the electric charge Q conserved in QED by $U(1)$ symmetry, the weak hypercharge ($Y = 2(Q - I_3)$) related to the electric charge and the weak isospin I_3) is conserved by the $U(1)_Y$ symmetry. The fermion fields are represented by the left-handed doublets χ_L and the right-handed singlets ψ_R, introduced in table 3. The doublet and singlet field for the first generation of leptons and quarks are,

$$\chi_L = \begin{pmatrix} \nu_e \\ e \end{pmatrix}_L \quad \& \quad \chi_L = \begin{pmatrix} u \\ d \end{pmatrix}_L$$

$$\psi_R = e_R \quad \& \quad \psi_R = u_R \ \& \ d_R$$

The Lagrangian for these fermion fields should be invariant under local gauge transformation corresponding to both $SU(2)_L$ and $U(1)_Y$ symmetry as,

$$\chi_L \rightarrow e^{i\beta(x)Y + i\alpha_a(x)\tau_a} \chi_L \tag{1.19}$$

$$\psi_R \rightarrow e^{i\beta(x)Y} \psi_R \tag{1.20}$$

where, $\beta(x)$ and $\alpha(x)$ are the local phase transformation for $U(1)_Y$ and $SU(2)_L$ symmetry groups respectively. Weak hypercharge operator Y and Pauli matrices $\tau_{a=1,2,3}$ are generators of $U(1)_Y$ and $SU(2)_L$ symmetry groups respectively. Similar to the formulation in QED and QCD discussed in Section 1.3.2 and 1.3.3, four new field strength tensors $B_{\mu\nu}$ and $W^a_{\mu\nu}$ corresponding to respectively the $U(1)_Y$ and $SU(2)_L$ transformations are introduced. The $SU(2)_L \otimes U(1)_Y$ gauge-invariant Lagrangian for a massless fermion and massless gauge fields is:

$$\mathcal{L}_0 = \bar{\chi}_L \gamma^\mu [i\partial_\mu - g\frac{\tau_a}{2}W^a_\mu + \frac{g'}{2}B_\mu]\chi_L + \bar{\psi}_R \gamma^\mu [i\partial_\mu + g'B_\mu]\psi_R - \frac{1}{4}W^a_{\mu\nu}W^{\mu\nu}_a - \frac{1}{4}B_{\mu\nu}B^{\mu\nu} \quad (1.21)$$

where similar to QED and QCD, the field strength tensors are defined in terms of the covariant derivative to preserve the gauge-invariance in the kinetic terms as,

$$B_{\mu\nu} = \partial_\mu B_\nu - \partial_\nu B_\mu \quad (1.22)$$

$$W^a_{\mu\nu} = \partial_\mu W^a_\nu - \partial_\nu W^a_\mu + g\epsilon^{abc}W^b_\mu W^c_\nu \quad (1.23)$$

The non-Abelian part of the $SU(2)_L$ transformation is represented by the last term of equation 1.23 which gives the quartic and triple self-interactions between the gauge bosons with coupling strength g.

The electroweak Lagrangian in equation 1.21 contains two terms, one of which gives rise to the charged-current interaction with the two $SU(2)$ boson field

$$W^\pm_\mu = \frac{W^1_\mu \mp iW^2_\mu}{\sqrt{(2)}} \quad (1.24)$$

via exchange of the $W^\pm$ bosons and the neutral current interactions from the two neutral gauge boson fields W^3_μ and B_μ.

The Lagrangian for the charged-current interaction for the first generation of quarks and leptons is,

$$\mathcal{L}_{CC} = \frac{g}{2\sqrt{2}}\{W_\mu^\dagger[\bar{u}\gamma^\mu(1-\gamma_5)d + \bar{\nu}_e\gamma^\mu(1-\gamma_5)e] \ + \ h.c\} \tag{1.25}$$

The $SU(2)_L$ charged-current interaction Lagrangian for the next two generations follows the same, establishing the universality of the quark and lepton interactions as a direct consequence of the gauge symmetry.

The neutral-current Lagrangian is given by,

$$\mathcal{L}_{NC} = \sum_j \bar{\psi}_j\gamma^\mu\{A_\mu[g\frac{T_3}{2}sin\theta_W + g'Ycos\theta_W] + Z_\mu[\frac{T_3}{2}cos\theta_W - g'Ysin\theta_W]\}\psi_j \tag{1.26}$$

where the two neutral gauge fields Z_μ and A_μ associated with Z boson and photon governing the weak neutral and electromagnetic interactions are obtained from an arbitrary linear combination of the W_μ^3 and B_μ fields as

$$\begin{pmatrix} A_\mu \\ Z_\mu \end{pmatrix} = \begin{pmatrix} cos\theta_W & sin\theta_W \\ -sin\theta_W & cos\theta_W \end{pmatrix} \begin{pmatrix} B_\mu \\ W_\mu^3 \end{pmatrix} \tag{1.27}$$

The following condition needs to be imposed to get QED from A_μ:

$$gsin\theta_W = g'cos\theta_W = e \ \& \ Y = Q - T_3 \tag{1.28}$$

, where $T_3 = \frac{\tau_3}{2}$ is the weak isospin and θ_W is the Weinberg mixing angle, which can be measured experimentally and expressed in terms of the two $SU(2)_L$ coupling g' and $U(1)_Y$ coupling g as:

$$sin\theta_W = \frac{g'}{\sqrt{g^2 + g'^2}} \ \& \ cos\theta_W = \frac{g}{\sqrt{g^2 + g'^2}} \tag{1.29}$$

The Lagrangian in equation 1.21 describes the electroweak interactions only for massless

fermions and massless gauge bosons, which contradicts the experimental observations. The mass origin of the fermions and gauge bosons is discussed in Section 1.3.5 below.

1.3.5 Higgs Mechanism

Massive gauge bosons in the Lagrangian 1.21 can be accommodated through the Brout-Englert-Higgs (BEH) mechanism, by introducing a complex scalar field ϕ in the spinor representation of $SU(2)_L$ doublet as [12],

$$\phi = \begin{pmatrix} \phi^+ \\ \phi^0 \end{pmatrix} \tag{1.30}$$

A new term in the SM Lagrangian $\mathcal{L}_{BEH}$ depending on this scalar field can be defined as,

$$\mathcal{L}_{BEH} = (D_\mu \phi)^\dagger (D^\mu \phi) - \mu^2 \phi^\dagger \phi + \lambda(\phi^\dagger \phi)^2 \tag{1.31}$$

The first term $(D_\mu \phi)^\dagger (D^\mu \phi)$ describes the kinematic of the new fields and the BEH potential $V(\phi)$ is given by the second term as,

$$V(\phi) = \lambda(\phi^\dagger \phi)^2 - \mu^2 \phi^\dagger \phi \tag{1.32}$$

The term $\lambda(\phi^\dagger \phi)^2$ describes the quartic self-interactions of the scalar fields and $\lambda > 0$ is imposed by the vacuum stability.

For $\mu^2 > 0$, the scalar field develops a nonzero Vacuum Expectation Value (VEV) which spontaneously breaks the symmetry. Due to the symmetry of $V(\phi)$ an infinite number of degenerate states exists with the potential v only depending on the combination of $\phi^\dagger \phi$ [13] with minimum energy satisfying $\phi^\dagger \phi = \frac{v^2}{2}$. This minimum energy requirement reduces one of the four degrees of freedom of the complex scalar field ϕ. The three remaining degrees of freedom can be eliminated by a gauge transformation. We can choose ϕ by eliminating the

upper component and the imaginary part of the lower component of the complex scalar field as,

$$< \phi >= \frac{1}{\sqrt{2}} \begin{pmatrix} 0 \\ v + H(x) \end{pmatrix}, \quad ;, \ H(x) = H^*(x) \frac{1}{\sqrt{2}} \begin{pmatrix} 0 \\ v \end{pmatrix} \tag{1.33}$$

where the Higgs field (H) emerges as the excitation from the vacuum state. This choice of the minimum, spontaneously breaks the gauge symmetry [14].

After substituting the ϕ in the Lagrangian in equation 1.31, the kinetic term takes the form

$$\begin{aligned} \mathcal{L}_{BEH \ Kinetic} = &\ \frac{\lambda}{2} v^4 \\ &+ \frac{1}{2} \partial_\mu H \partial^\mu H - \lambda v^2 H^2 + \frac{\lambda}{\sqrt{2}} v H^3 + \frac{\lambda}{8} H^4 \\ &+ \frac{1}{4} (v + \frac{1}{\sqrt{2}} H)^2 (W^1_\mu \ W^2_\mu \ W^3_\mu \ B_\mu) \begin{pmatrix} g^2 & 0 & 0 & 0 \\ 0 & g^2 & 0 & 0 \\ 0 & 0 & g^2 & gg' \\ 0 & 0 & gg' & g^2 \end{pmatrix} \begin{pmatrix} W^{1\mu} \\ W^{2\mu} \\ W^{3\mu} \\ B^\mu \end{pmatrix} \end{aligned} \tag{1.34}$$

where, the first line is the vacuum energy density and can be ignored in the case of QFT. The second line describes the triple and quartic self-interactions of the Higgs field as well as the mass term of the real scalar field H as $m_H = 2\lambda v^2$. The last line contains the mass term for the vector bosons.

From equations 1.34 and 1.24 is evident the mass of the two charged vector bosons $W^\pm$ is $m_W = \frac{1}{2} g^2 v^2$. Similarly, from equations 1.34 and 1.27, mass of the Z boson is $m_Z = \frac{1}{2} (g^2 + g') v^2$ and mass of the photon is $m_\gamma = 0$.

The initial $SU(2)_L$ Lagrangian in equation 1.31 started with four gauge symmetries, which is reduced to a single $U(1)_Q$ gauge symmetry associated with the massless vector field in equation 1.34. This phenomenon in the Higgs mechanism is called the Electroweak

Symmetry Breaking (EWSB) mechanism. As discussed above, the EWSB mechanism is at the heart of the SM by which the gauge boson gets the mass which also arises the longitudinal polarization of the massive vector bosons. This thesis summarizes a measurement that has an experimental sensitivity to a such important property of the theory.

The last remaining piece in the SM is adding the fermion mass to the Lagrangian. A simple Lagrangian with the fermion mass can be written as,

$$\mathcal{L}_{mass\ fermion} = -m(\bar{\chi}_L\psi_R + \bar{\psi}_R\chi_L) \tag{1.35}$$

This term violates $SU(2)_L$ gauge symmetry because the left-handed fermions are doublets and the right-handed are singlets. Adding a scalar complex field $\phi = \frac{1}{\sqrt{2}}\begin{pmatrix} 0 \\ v + H(x) \end{pmatrix}$ in the Lagrangian becomes,

$$\mathcal{L}_{Yukawa,\ \ell} = \frac{G_\ell v}{\sqrt{2}}(\bar{\chi}_L\psi_R + \bar{\psi}_R\chi_L) - \frac{G_\ell}{\sqrt{2}}(\bar{\chi}_L\psi_R + \bar{\psi}_R\chi_L)H \tag{1.36}$$

with arbitrary parameters $G_{\ell=e,\mu,\tau}$. The constant in the first term $\frac{G_\ell v}{\sqrt{2}}$ represents the mass of the fermions, whereas the second term gives the interaction of fermions with the Higgs field.

Similarly, the mass terms for quarks follow but including the down-type quarks, the parameters corresponding to G_ℓ are matrices G_q^{ij} for the quark families i, j and up-type and down-type quarks as:

$$\mathcal{L}_{Yukawa,\ Q} = -G_d^{ij}(\bar{u}_i, \bar{d}_i)_L\phi d_{jR} - G_u^{ij}(\bar{u}_i, \bar{d}_i)_L\phi u_{jR} + h.c. \tag{1.37}$$

The final Standard Model Lagrangian is the sum of the QED (equation 1.9), QCD (equation 1.16), Boson self-interactions (equation 1.21), Higgs potential and self-interactions (equation 1.31), and the Higgs-fermion Yukawa coupling (equations 1.36 & 1.37), which in a compact form is written in equation 1.1.

17

2 Limitations of the Standard Model

The predictions of the Standard Model have been experimentally validated by many discoveries since the 20th century. The breakthrough discovery of the Higgs boson in 2012 at the LHC validated the last piece of the theory [15]& [16]. Many predicted parameters such as production cross-sections and decay branching ratios for several processes have been measured with high precision. No statistically significant discrepancy from theory has been observed except for the $W^{\pm}$ boson mass measurement from the CDF II Collaboration [17].

Despite the incredible success of the theory, experimental evidence suggests that the theory is incomplete. SM has the following limitations:

- SM fails to explain the gravitational force.

- SM only describes 5% of the universe. It fails to explain dark matter whose existence is experimentally supported by astrophysical observations such as galactic rotation curves and gravitational lensing [18]. It also doesn't explain dark energy.

- The CP violation allowed in SM cannot explain the amount of anti-matter asymmetry observed in the universe.

- The strengths of the four fundamental forces are different by many orders of magnitude. It is not yet understood the hierarchy of such interactions.

These limitations suggest that the SM is an effective field theory, only describing an approximation of our universe. Thus, motivating the experimental searches for new physics beyond the Standard Model (BSM).

3 Phenomenology of Proton-Proton Collisions

The main results discussed in this thesis are differential cross-sections for di-Z boson production in association with two jets in a proton-proton collider at the center of mass energy of $\sqrt{s} = 13\ TeV$. Protons are composite particles made up of quarks and gluons. Thus the theoretical formalism discussed above doesn't provide all the necessary tools for experimental cross-section measurements in hadron colliders. The differential cross-section $d\sigma$ for two particles is given by,

$$d\sigma = \frac{|\mathcal{M}|^2}{F} dQ \tag{3.1}$$

where F is the incident flux and dQ represents the Lorentz invariant phase space factor. The scattering amplitude $\mathcal{M}$ is the matrix element calculated from the Lagrangian density of the SM using a perturbative expansion [19].

The cross-section of a process with two initial-state partons p_1 and p_2 producing the final state X is given by:

$$d\sigma_{p_1 p_2 \to X} = \int dx_1 dx_2 \sum_{q_1, q_2} f_{q_1}(x_1, \mu_F) f_{q_2}(x_2, \mu_F) d\sigma_{q_1 q_2 \to X}(x_1, x_2, \mu_F, \mu_R) \tag{3.2}$$

where, q_1, q_2 are the partons of the protons, and $d\sigma_{q_1 q_2 \to X}(x_1, x_2, \mu_F, \mu_R)$ is the partonic cross-section. The functions $f_{q_1}(x_1, \mu_F)$ & $f_{q_2}(x_2, \mu_F)$ are the parton distribution functions (PDF) representing the density of the partons q inside a proton carrying the longitudinal momentum fraction x. The PDFs are determined experimentally using data from deep-inelastic-scattering, jets production, and Drell Yan events [20] [21]. As shown by figure 2, a PDF of a parton depends on the reference value of the momentum transfer Q_0^2. The differences are driven by modifications of the partons' momenta resulting from the emission of gluons off of quarks and the splitting of gluons to $q\bar{q}$ pairs. A PDF at any value of Q^2 can be calculated using the PDF at reference scale Q_0^2. The factorization scale μ_F determines
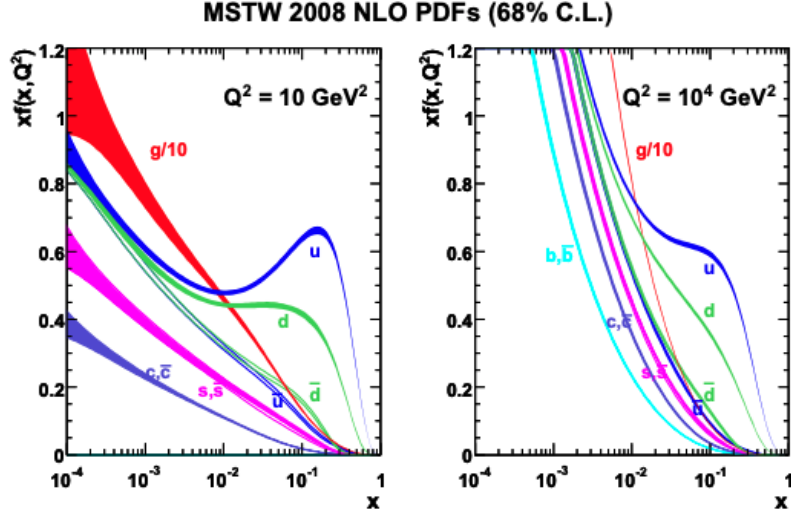
Figure 2: Parton distribution functions $xf_q(x, Q^2)$ for reference momentum transfer $Q_0^2 = 10\ GeV^2$ (left) and $Q_0^2 = 10^4\ GeV^2$ (right). The dependence of momentum fraction z carried by a parton is extracted in global PDF fits from experimental data [4].

the threshold whether the perturbative corrections modify the PDF or are included in the partonic cross-sections $d\sigma_{q_1 q_2}$ [19].

The partonic cross-section is calculated perturbatively as an expansion in terms of the strong coupling constant α_S as,

$$d\sigma_{q_1 q_2 \to X} = \alpha_S^k \sum_{m=0}^{n} c_m \alpha_S^m \qquad (3.3)$$

The coefficient c_m depends on the center-of-mass energy s and theoretical calculations usually contain a finite number of coefficients. Leading order (LO) calculations include one term ($n = 0$), whereas next-to-leading order (NLO) and next-to-next-to-leading order (NNLO) contains two ($n = 1$) and three ($n = 2$) terms respectively. The theoretical calculations relevant to the thesis are generally calculated at NLO. The higher-order terms in the series contain additional virtual loop contributions and real emissions of quarks and gluons. The presence of virtual loops beyond the LO introduces singularities in the calculation of scattering amplitudes. The divergences are controlled via the renormalization procedure, where the

20

singularities are absorbed by reparametrization of the coupling and mass parameters. The renormalization process is energy-dependent. Therefore, the predicted cross-sections from theoretical calculations are dependent on the renormalization scale μ_R and factorization scale μ_F. The scale dependence is varied in Monte Carlo simulations to derive uncertainties on the predicted cross-section due to missing higher-order contributions.

The additional partons of the two protons that interact in the hard interaction process lead to minor energy deposits in the detector referred to as an underlying event. Any outgoing partons from the interaction emit multiple QCD radiation via the parton showering process, where the energy of each parton is split among an increasing number of other elementary particles. Due to the color confinement nature of QCD, at lower energies of the order of the pole of the QCD running coupling (λ_{QCD}), the partons are bound into stable and unstable hadrons. This process is named as hadronization and leads to the formation of collimated sprays of charged and neutral hadrons in the detector called jets. Figure 3, shows schematically the phenomenology of di-Z boson production in association with two jets in the proton-proton collider. The theoretical predictions of such events are calculated using Monte Carlo (MC) simulations which include matrix element calculations for two partons giving two Z bosons, the parton showering, the effect of the underlying events, hadronizations, and pile-up. A comprehensive overview of the methods used in MC simulation is discussed in Ref [22].
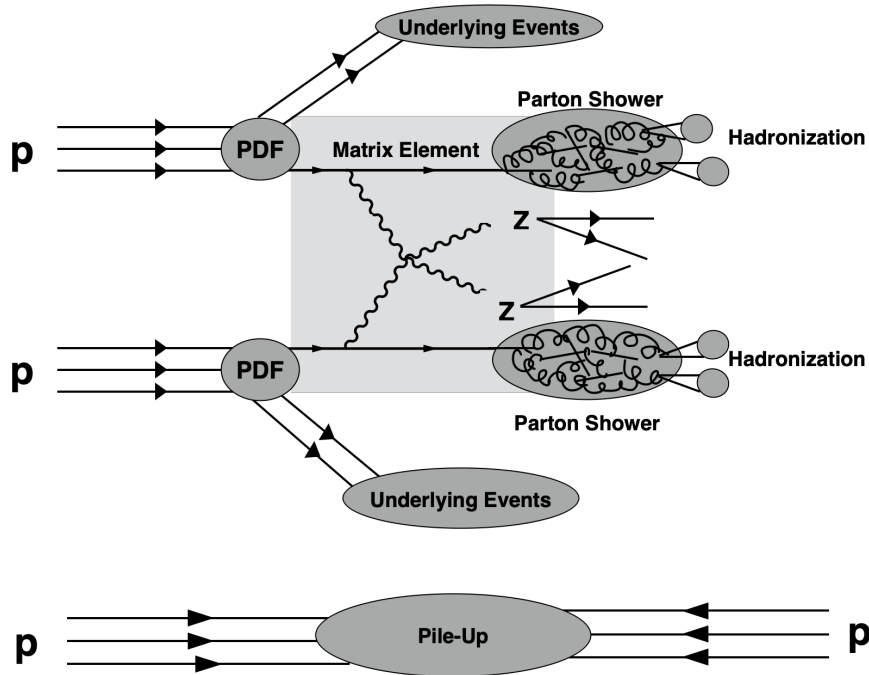
Figure 3: Phenomenology of di-Z boson production in association with two jets in proton-proton collider

4   Electroweak Diboson Physics

In LHC, two types of physics processes, the QCD production at the order $\alpha_S^2 \alpha_{EWK}^4$ and the EWK production at order α_{EWK}^6 contribute to the production of di-Z bosons in an association of two jets ($ZZjj$) [23]. Figures 4 and 5 shows the Feynman diagram at leading order for the QCD ZZjj process, whereas figure 6 shows the Feynman diagram at leading order for the EWK production of ZZjj [24]. The EWK production consists of two sets of interactions, first, the Vector Boson Scattering processes involving either triple (figure 6a) or quartic (figure 6b) self-interactions of the gauge-bosons, and second the diagrams featuring the Higgs bosons (figure 6c & 6d). The scattering amplitudes of the VBS processes involving longitudinally polarized vector bosons, grow quadratically with the center of mass energy ($\sqrt{s}$), eventually violating the unitarity bounds. The precise SM interference between the Higgs-featured process and the VBS process restores the unitarity [25]. As discussed in Section 1.3.5, the massive W and Z bosons get their masses via the BEH mechanism through EWSB. As a consequence of EWSB, the W and Z bosons acquire an additional degree of freedom (the longitudinal polarization mode) whose scattering interfere with the Higgs featured processes. Thus, the study of electroweak production of the di-Z bosons in association with two jets provides a direct probe of the EWSB, which is at the heart of the SM [23].
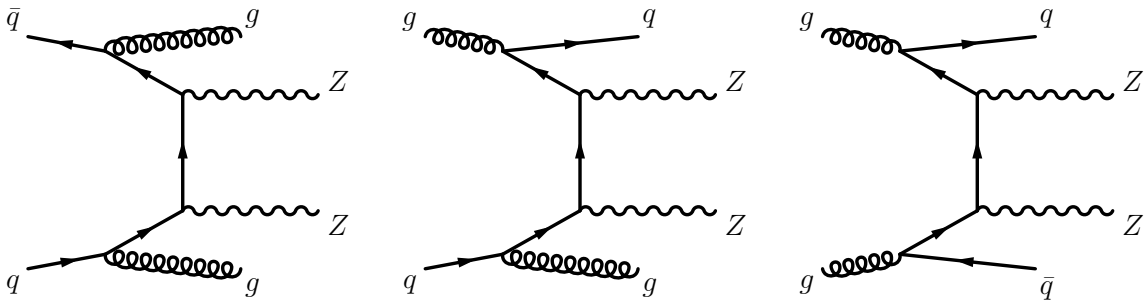

Figure 4: Typical diagrams of LO qq and gg induced QCD $\alpha_S^2 \alpha_{EWK}^4$ production of $ZZjj$.
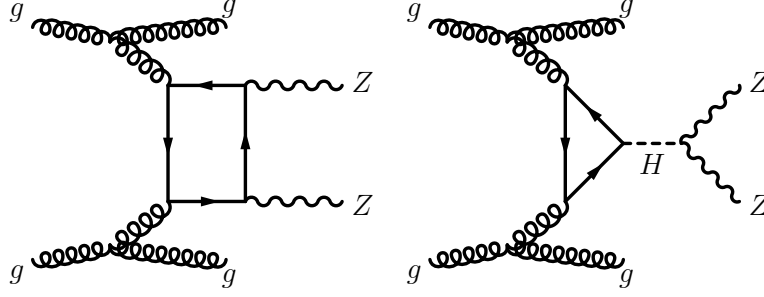
Figure 5: Typical diagrams for LO gg loop induced the QCD $\alpha_S^4 \alpha_{EWK}^4$ production of $ZZjj$.

The triple and quartic self-interactions of the gauge bosons arise from the square of the non-Abelian structure of $SU(2)$ in the kinetic term $\frac{1}{4}W_{\mu\nu}^a W_a^{\mu\nu}$ of the EWK Lagrangian in equation 1.21. Implementing the values of the field strength tensor $W_{\mu\nu}^a$ from equation 1.23, the relations of $W_\mu^\pm$ fields in equation 1.24, and the relations of neutral gauge fields in equation 1.27, the triple and quartic self interaction terms become,

$$\mathcal{L}_3 = ie_{V=\gamma,Z}[W_{\mu\nu}^+ W^{-\mu}V^\nu - W_{\mu\nu}^- W^{+\mu}V^\nu + W_\mu^+ W_\nu^- V^{\mu\nu}] \tag{4.1}$$

$$
\begin{aligned}
\mathcal{L}_4 = {} & e_W^2[W_\mu^- W^{+\mu}W_\nu^- W^{+\nu} - W_\mu^- W^{-\mu}W_\nu^+ W^{+\nu}] \\
& + e_{V=\gamma,Z}^2[W_\mu^- W^{+\mu}V_\nu V^\nu - W_\mu^- V^\mu W_\nu^+ Z^\nu] \\
& + e_\gamma e_Z[2W_\mu^- W^{+\mu}Z_\nu A^\nu - W_\mu^- Z^\mu W_\nu^+ A^\nu - W_\mu^- A^\mu W_\nu^+ Z^\nu]
\end{aligned}
\tag{4.2}
$$

where, $e_\gamma = gsin\theta_W$; $e_W = \frac{e_\gamma}{2\sqrt{2}sin\theta_W}$ & $e_Z = e_\gamma cot\theta_W$ are the precise coupling strengths for vector boson self-interaction. Both triple and quartic neutral couplings such as ZZZ or $ZZZZ$ are absent in the SM.

Similarly, the couplings of Higgs to vector bosons are also predicted precisely by the BEH mechanism in equation 1.34 as:

$$\mathcal{L}_{HVV} = \frac{m_W^2}{v^2}W_\mu^+ W^{-\mu}h^2 + \frac{m_Z^2}{v^2}Z_\mu Z^\mu h^2 \tag{4.3}$$

24
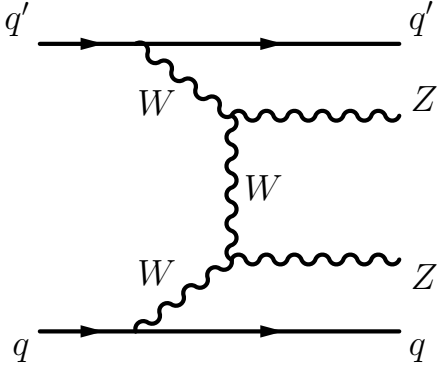
(a) ZZjj production with two triple gauge cou-
pling (TGC) vertices.
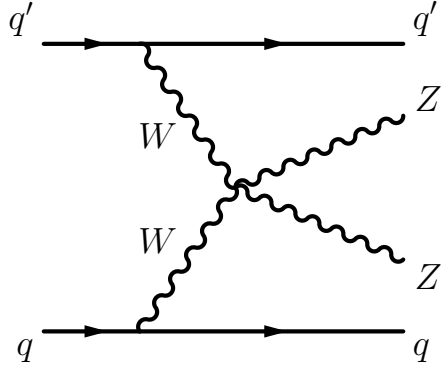
(b) ZZjj production with a quartic gauge cou-
pling (QGC) vertex.
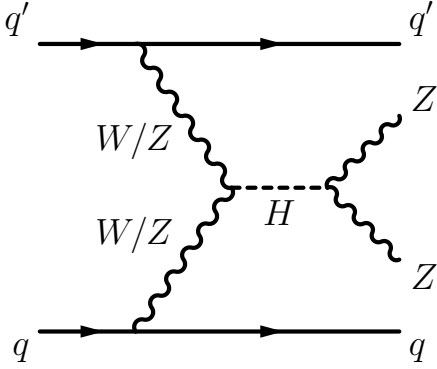
(c) s-channel Higgs ZZjj Production.
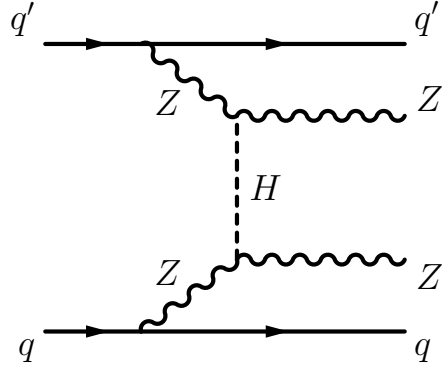
(d) t-channel Higgs ZZjj Production.

Figure 6: Feynman diagrams at LO for the EWK α_{EWK}^6 production of $ZZjj$.

The EWK production of $ZZjj$ is extremely sensitive to any possible anomalous triple gauge couplings (aTGC), anomalous quartic gauge couplings (aQGC), or anomalous Higgs to vector boson coupling [26] [27] [28] . Therefore, it is imperative to probe the high energy behavior of the EWK production of $ZZjj$ to seek possible deviations arising from the physics processes beyond the Standard Model (BSM).

The EWK $ZZjj$ production with each Z boson decaying to a pair of same-flavor opposite-sign (SFOS) lepton pairs is an extremely rare process. Moreover, with limited statistics in Run-2 the QCD background processes dominate the $ZZjj \to 4\ell jj$ final state [29]. There-

fore, the differential cross-sections discussed in this thesis are measured in a VBS-enhanced phase space with a high fraction of events resulting from the EWK $ZZjj$ process. The enhanced phase space relies on the characteristic feature of the EWK process with two jets (jj) in the forward-backward region originating from the scattered quarks. These jets have large rapidity separation with no additional hadronic activity from the hard scattering between the two jets [30]. The decay of the two Z bosons into SFOS muons or electron pairs defines the final signature of the VBS-$ZZjj$-like event.

Chapter III: The Large Hadron Collider

5 ATLAS Detector

6 Physics Object Reconstruction

6.1 Electrons

6.2 Muons

6.3 Jets

7 Future Upgrades

Chapter IV: Analysis Overview

8   Goals

The primary goal of the analysis is to measure the differential cross-sections of the kinematic observables that are sensitive to the EWK $ZZjj \rightarrow 4\ell jj$ production mode. The differential cross-sections measured in VBS-enhanced phase space are used in the precision study of the SM $4\ell jj$ production and to put constrain on the BSM physics. For simpler re-interpretation in the future without ATLAS detector simulations, the differential cross-sections are measured at a particle level using an unfolding technique, which corrects for the detector effects. The details of the unfolding to extrapolate the particle-level yield from detector-level yield will be discussed in section 15. The unfolded cross-sections shown in section 17 are then used to constrain the effect of BSM in a model-independent framework using the Effective Field Theory (EFT) approach which will be discussed in section 18.

9 Phase Space Definition

The unfolded differential cross-sections are measured in a phase space within the acceptance of the detector. This section summarizes the selections defining the fiducial phase space of the analysis.

9.1 Fiducial Volume

The fiducial phase space consists of events with $pp \to ZZjj \to 4\ell jj$ ($\ell = e,\ \mu$) with four centrally produced prompt-leptons and two jets with large rapidity gap as motivated by section 4. The fiducial phase space doesn't contain any leptons from the decays of unstable taus. Both particle-level electrons and muons are required to be at a dressed level. Dressed leptons in MC generators are constructed by adding the four-momenta of nearby photons emitted by the lepton within a cone size of $\Delta R < 0.1$.

To ensure the selected events fall within detector acceptance, several kinematic cuts summarized in Table 4 are applied to indvidually to the muons, electrons, and jets before defining the event quadruplet and dijet. Each electrons are required to have $p_T > 7$ GeV and $|\eta| < 2.47$, whereas the muons satisfy $p_T > 5$ GeV and $|\eta| < 2.7$. Lepton quadruplets are formed by requiring two same-flavor, opposite-charge (SF-OC) lepton pairs, with leading and sub-leading lepton $p_T > 20$ GeV and angular separation between any two leptons to satisfy $\Delta R > 0.05$. Additionally, the invariant mass of any SF-OC lepton pair is required to satisfy $m_{\ell\ell} > 5$ GeV to suppress the contamination from lower resonance backgrounds. Based on these requirements, the quadruplets can be of the following three types:

- $4e$: events with two e^+e^- pairs.

- 4μ: events with two $\mu^+\mu^-$ pairs.

- $2e2\mu$ or $2\mu2e$: events where one of the pair is e^+e^- and other is $\mu^+\mu^-$

In any event with more than two SF-OS lepton pairs, the quadruplet is formed by choosing the two pairs that minimize the distance to the Z resonance pole. Once the quadruplet is formed, the leading-lepton pair is defined as the one having a higher value of absolute rapidity i.e. $|y_{ij}|$. Finally, an additional criterion of $m_{4\ell} > 130$ GeV is imposed on the invariant mass of the quadruplet.

Similarly, the di-jet in the fiducial phase space are also constructed from the leading-dressed jets with opposite sign of pseudo-rapidity (η) to imitate the detector-level VBS di-jet production where jets are reconstructed on the opposite side of the detector. The jets are required to satisfy $|n| < 4.5$, $p_{T, \text{ leading jet}} > 40$ GeV, and $p_{T, \text{ sub}-\text{leading jet}} > 30$ GeV. The di-jet is required to have a large rapidity separation of $|\Delta y_{jj}| > 2$ and $m_{jj} > 300$ GeV to resemble dijet produced in electroweak $ZZjj$ production. The requirements imposed on the quadruplet and the di-jet are summarized in Table 5

Table 4: Details of the kinematic pre-selection applied to the dressed baseline electrons, muons and jets.

Selections	Electrons	Muons	Jets
p_T	> 7 GeV	> 5 GeV	> 30GeV
$|\eta|$	< 2.47	< 2.7	< 4.5

Table 5: Details of the selections applied to form a quadruplet and a dijet selection in the fiducial volume.

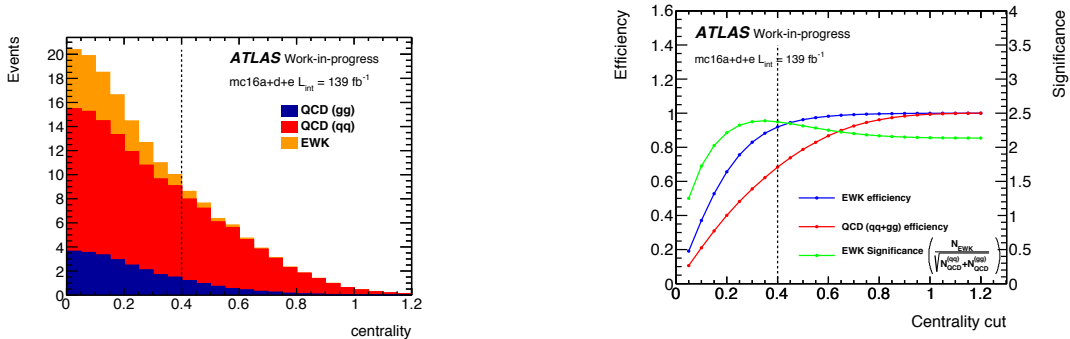| Selections	Cut
Lepton Kinematics	$P_{T, \text{ leading lepton}} > 20$ GeV $P_{T, \text{ sub}-\text{leading lepton}} > 20$ GeV
Pair Requirement	$\Delta R_{\ell i, \ell j} > 0.05$ SF-OC with $m_{\ell\ell} > 5$ GeV
Quadruplet Requirement	2 pair candidates with smallest $|m_{12} - m_Z| + |m_{34} - m_Z|$ Leading pair: pair with highest $|y_{ij}|$ Sub-leading pair: pair with lowest $|y_{ij}|$ $m_{4\ell} > 130$ GeV
Di-jet Requirement	$p_{T, \text{ leading jet}} > 40$ GeV $|\Delta y_{jj}| > 2$ $m_{jj} > 300$ GeV

9.2 Signal Region

The signal region of the analysis is defined based on the centrality (ζ) of the di-Zboson production in an event. Centrality depends on the rapidity of the quadruplet and the rapidity of the dijet as:

$$\zeta = \frac{\left|y_{quadruplet} - 0.5 * \left(y_{leading\ jet} + y_{sub-leading\ jet}\right)\right|}{\left|y_{leading\ jet} - y_{sub-leading\ jet}\right|} \tag{9.1}$$

Figure 7a shows the distribution of centrality in MC for the three main production modes of $ZZjj$. The cut value on the $ZZjj$ centrality is chosen to maximize the significance of the EWK component over the inclusive qq and gg-initiated QCD production (defined as $s = \frac{N_{EWK}}{\sqrt{N_{QCD}^{(qq)} + N_{QCD}^{(gg)}}}$), while maintaining a good selection efficiency of EWK events. The second distribution in 7b shows the efficiency and significance for various cut values.

A VBS-enhanced signal region is defined based on events with a quadruplet, a dijet, and $\zeta < 0.4$. The low value of the centrality and the requirements for a signal dijet ensures the events in this signal region originate in a larger fraction from the electroweak production of ZZjj. Additionally, a VBS Suppressed control region is defined based on events with a quadruplet, a dijet, and $\zeta > 0.4$. These events mostly originate from the QCD production of ZZjj and are used to optimize the analysis strategies.

(a) Yields of EWK(red) and QCD (qq-initiated in blue, gg-initiated in greed) ZZjj production as a function of centrality.

(b) Selection efficiency (EWK in blue, QCD in red) and EWK significance (green) for different centrality cut values. The selected cut values of 0.4 are highlighted with a dashed line.

31

10 Reconstruction Selection

This section summarizes the detector-level phase space selections applied to three physics objects, electrons, muons, and jets used in the measurement. Each object is categorized into two types: *baseline* and *signal*. Physics objects satisfying a set of kinematic selections or looser identification criteria are categorized as *baseline*. *Signal* objects are a subset of the baseline leptons passing either stricter kinematic selections or additional isolation and track-to-vertex association (TTVA) requirements.

10.1 Electrons

As discussed in Section 6.1 electrons are reconstructed by matching the inner detector track (ID) to an energy cluster in the electromagnetic calorimeter. Baseline electron objects are required to satisfy the kinematic selections of $p_T > 7$ GeV & $|\eta| < 2.47$ and a loose likelihood identification of working point *LHVeryLoose*. To avoid the electrons from pileup, a loose vertex association requirement of $|z_0 sin\theta| < 0.5$ mm and an overlap removal discussed in section 10.4 is applied to the baseline electron candidates.

Signal electrons are required to pass a more stringent loose likelihood identification "LHLooseBL" which requires at least one hit in the innermost layer of the pixel detector. The signal electrons are distinguished by requiring the baseline electrons to have impact parameter requirements of $d0/\sigma_{d0} < 5$ and an isolation working point identification of "LooseVarRad". Table 6 summarizes the several selections imposed to define the baseline and signal electrons.

10.2 Muons

As discussed in section 6.2, muons are reconstructed in multiple ways based on information from the inner detector (ID), the muon spectrometer (MS), and the calorimeters. All baseline muons are required to satisfy $|\eta| < 2.7$, $p_T > 5$ GeV, a loose impact parameter requirements

Table 6: Definition of the baseline and signal electrons.

Selection Category	Baseline	Signal
Kinematic cuts	$p_T > 7$ GeV $\|\eta\| < 2.47$	$p_T > 7$ GeV $\|\eta\| < 2.47$
Identification	LHVeryLoose	LHLooseBL
Vertex Association	$\|z_0 sin\theta\| < 0.5$ mm	$\|z_0 sin\theta\| < 0.5$ mm
Overlap removal	Lepton-favored	Lepton-favored
Isolation Working Point	–	LooseVarRad
Impact Parameters	–	$d_0/\sigma_{d_0} < 5$

of $\|z_0 sin\theta\| < 0.5$ mm, lepton-favoring overlap removal and *Loose* identification working point. The signal muons are identified by requiring additional isolation identification of "PflowLooseVarRad" and TTVA requirements of $d_0/\sigma_{d_0} < 3$. Table 7 summarizes baseline and signal muons selection requirements.

Table 7: Definition of the baseline and signal muons.

Selection Category	Baseline	Signal
Kinematic cuts	$p_T > 5$ GeV Calo-tagged $p_T > 15$ GeV $\|\eta\| < 2.7$	$p_T > 5$ GeV Calo-tagged $p_T > 15$ GeV $\|\eta\| < 2.7$
Identification	Loose	Loose
Vertex Association	$\|z_0 sin\theta\| < 0.5$ mm	$\|z_0 sin\theta\| < 0.5$ mm
Overlap removal	Lepton-favored	Lepton-favored
Isolation Working Point	–	PflowLooseVarRad
Impact Parameters	–	$d_0/\sigma_{d_0} < 3$

10.3   Jets

Jets are reconstructed with the particle flow anti$-K_T$ clustering algorithm using a radius parameter of $R = 0.4$ as discussed in section 6.3. The jets reconstructed using the particle flow algorithm are required to satisfy $p_T > 15$ GeV, $\|\eta\| < 4.5$ kinematic cuts and the lepton-favored overlap removal to be classified as baseline jets. Baseline jets satisfying the *Tight* working point of the jet to the vertex tagger tool are classified as signal jets. *Jet-vertex-tagger (JVT)* is applied to the baseline jets with $\|\eta\| < 2.4$ whereas the textitforward-jet-

vertex-tagger (fJVT) tool is applied to the baseline jets with $|\eta| > 2.5$. Table 8 summarizes the details of baseline and signal jets selection.

Table 8: Definition of the baseline and signal jets.

Selection Category	**Baseline**	**Signal**
Kinematic cuts	$p_\mathrm{T} > 30$ GeV	$p_\mathrm{T} > 30$ GeV
	$|\eta| < 4.5$	$|\eta| < 4.5$
Identification	AntiKt4EMPFlow	AntiKt4EMPFlow
Overlap removal	Lepton-favored	Lepton-favored
Jet-Vertex-Tagger	$-$	$|\eta| < 2.4$ JVT ("Tight")
	$-$	$|\eta| > 2.5$ fJVT ("Tight")

10.4   Overlap Removal

To remove the physics objects reconstructed from the same detector signal, an overlap removal procedure is applied. The measurement used a lepton-favored overlap removal which selects leptons over jets. Overlap removal is an iterative process in which only objects surviving all previous steps are used in the subsequent steps. A summary of the overlap removal steps is shown in table 9, where the ΔR is the angular separation between objects calculated using rapidity.

Table 9: Overlap removal used in the analysis. If an object is marked to be removed in one step, it does not enter into the subsequent step.

Remove Object	Accept Object	Overlap Criteria
Electron	Electron	Share a track or have overlapping calorimeter cluster. Keep electron with higher p_T
Muon	Electron	Share ID track and the muon is calo-tagged
Electron	Muon	Share ID track
Jet	Electron	$\Delta R_{e-jet} < 0.2$
Jet	Muon	$\Delta R_{\mu-jet} < 0.2$/ghost-associated and $N_{jet\ tracks} < 3$

11   Event Selection

12 Datasets and Monte Carlo Simulation

12.1 LHC Dataset

The measurement uses the LHC collision data, named the ATLAS Run-2 dataset collected by the ATLAS experiment during its operation in 2015, 2016, 2017, and 2018. This dataset corresponds to proton-proton collisions at the center-of-mass energy of $\sqrt{(s)} = 13$ TeV and total integrated luminosity of 139 ± 2.4 fb^{-1} measured by the LUCID-2 detector [31] [5]. The uncertainty, on the integrated luminosity, is obtained by combining the measurements of LHC runs each year. Each data-taking run period is further divided into sub-periods of one to three weeks that vary in beam and detector conditions. The dataset used in physics analyses is required to satisfy a series of data quality checks discussed in detail in Ref [32]. The data passing these requirements collectively form a Good Run List (GRL) which consists of several luminosity blocks (LB). Figure 8 shows the total integrated luminosity delivered by LHC in the green distribution, recorded by the ATLAS experiment in the yellow distribution and part of the GRL in the blue distribution. The plateaus correspond to the end-of-year shutdowns of LHC and the slopes correspond to the increasing instantaneous luminosity in different data-taking periods.

Following data samples from the GRL are used for this measurement,

- GoodRunsLists/data15_13TeV/20170619/PHYS_StandardGRL_All_Good_25ns_276262-284484_OflLumi-13TeV-008.root

- GoodRunsLists/data16_13TeV/20180129/PHYS_StandardGRL_All_Good_25ns_297730-311481_OflLumi-13TeV-009.root

- GoodRunsLists/data17_13TeV/20180619/physics_25ns_Triggerno17e33prim.lumicalc.OflLumi-13TeV-010.root

- GoodRunsLists/data18_13TeV/20180924/physics_25ns_Triggerno17e33prim.lumicalc.OflLumi-13TeV-001.root
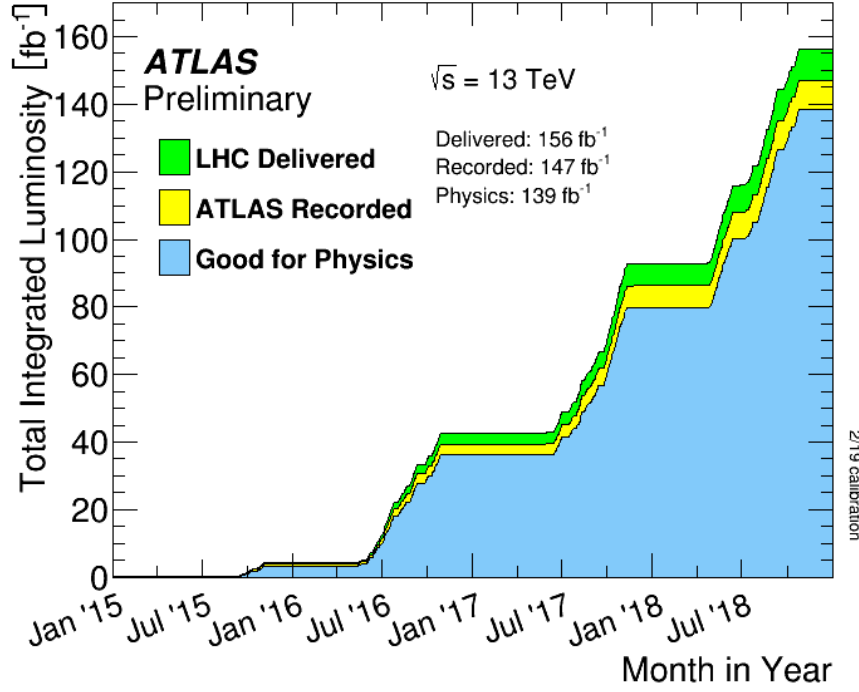
Figure 8: Total integrated luminosity collected during data taking period in Run-2 [32].

12.2 Monte Carlo Samples

As briefly mentioned in Section 3, the $pp \rightarrow ZZjj \rightarrow 4\ell jj$ events are generated using an MC generator that incorporates the matrix element calculations for the hard-scatter $ZZjj \rightarrow 4\ell jj$ production, the parton showering, hadronization, the effect of the underlying events, and pile-up. The generated events then are simulated to interact with the ATLAS material using the Geant4 simulation toolkit following the description in Ref [33]. The energy deposits of the simulated events in the detectors are then digitized and reconstructed using a detector geometry corresponding to the data-taking period. A schematic overview of the MC generation is shown in figure 9.

12.2.1 Signal Samples

As discussed in section 4, two types of interaction, QCD and EWK give us $pp \rightarrow ZZjj \rightarrow 4\ell jj$ final state. The two types of QCD process, quark induced $qqZZ$ ($qq \rightarrow ZZ^* \rightarrow 4\ell jj$)
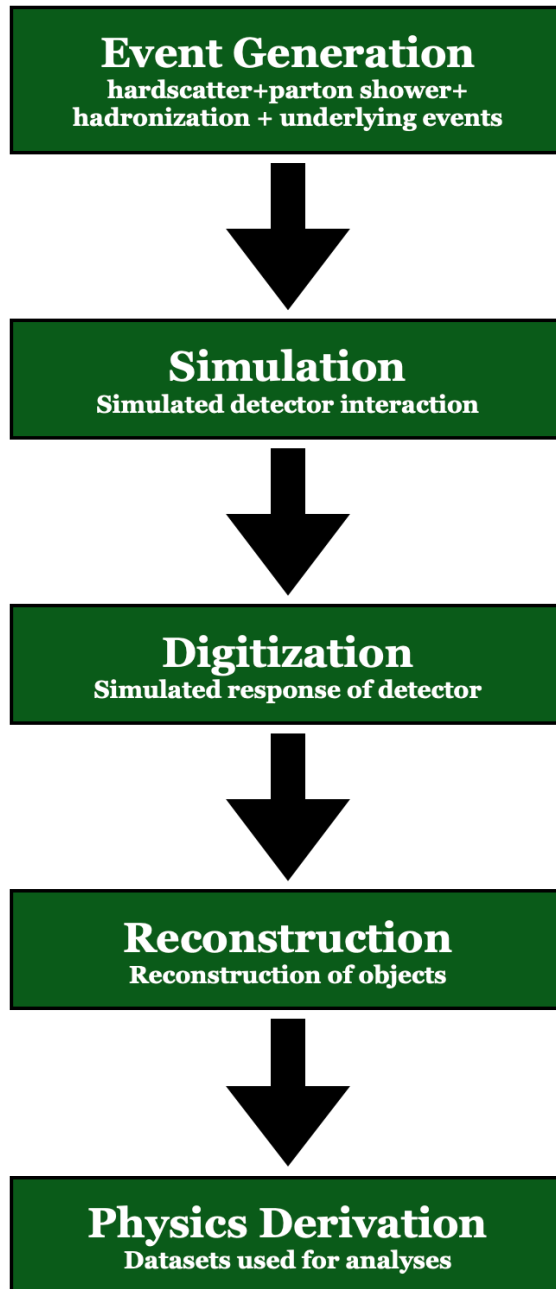
Figure 9: Various steps in MC sample generation.

and gluon induced $ggZZ$ ($gg \to ZZ^* \to 4\ell jj$) are simulated using the SHERPA 2.2.2 MC generator. The $qqZZ$ and $ggZZ$ samples corresponding to figure 4 are generated with NLO accuracy in QCD up to one additional parton emission and LO accuracy for up to three additional partons emission. The loop-induced $ggZZ$ samples emerging at NNLO in α_S corresponding to figure 5 are generated using LO-accurate matrix elements for up to one additional parton emission [34]. The generator uses an NNPDF3.0NNLO PDF set evaluated using different measurements from several experiments such as deep-inelastic inclusive cross-sections measurement from HERA-II, the combined charm data from HERA, jet production, vector boson rapidity and transverse momentum measurements from ATLAS, CMS and LHCb, total cross sections of top quark pair production from ATLAS and CMS and W+c data from CMS [35]. Parton showering is done by SHERPA's internal algorithm based on Catani–Seymour dipole factorization matrix element [36]. The matrix element calculations are matched and merged using the $ME + PS@NLO$ prescription [37].

An alternative MADGRAPH5 samples are also used in the measurement for the parton induced $qqZZ$ samples which are produced at NLO accuracy for up to one additional parton emission and LO accuracy for up to three additional parton emission [38]. The generator uses A14NNPDF23LO PDF set and the ME is interfaced with PYTHIA8 for parton showering, merging and matching [39].

The EWK production $qqZZjj$ ($qq \to ZZ^{(*)}jj \to 4\ell jj$) is simulated using a POWHEG-V2 generator using an MSTW2008 PDF set with NLO accuracy in QCD correction and interfaced with Pythia8 for parton showering and hadronization [40]. An alternative sample at LO accuracy is also used in the measurement from MADGRAPH5 with A14NNPDF23LO PDF set and PYTHIA8 showering [38]. The signal MC samples used in the measurement are summarized in Table 10

Process	Description	Generator	PDF	Accuracy
QCD				
$q\bar{q} \to ZZ^{(*)} \to 4\ell$	inclusive	SHERPA2.2.2 MADGRAPH	NNPDF3.0NNLO A14NNPDF23LO	$0, 1j@NLO + 2, 3j@LO$
QCD gg loop $gg \to ZZ^{(*)} \to 4\ell$	$m_{4\ell} > 130$ GeV	SHERPA2.2.2	NNPDF3.0NNLO	$0, 1j@LO$
EWK $q\bar{q} \to ZZ^{(*)}jj \to 4\ell jj$	$m_{4\ell} > 130$ GeV	PYTHIA8 MADGRAPH	MSTW2008 A14NNPDF23LO	$\geq 2j$ (EWK) @ NLO QCD $\geq 2j$ (EWK) @LO

Table 10: List of signal MC samples used in the analysis. Each process consists of three different generation campaigns corresponding to the data-taking conditions of the ATLAS Run2 data-taking periods.

12.2.2 Background Samples

In addition to the QCD and EWK production discussed above two other processes, triboson (WWZ, WZZ, ZZZ) and Z-bosons production in association with top quark pair ($t\bar{t}Z$) also contributes to the $ZZjj \to 4\ell jj$ final state. The triboson processes are modeled with SHERPA2.2.2 generator at NLO accuracy in QCD for zero or one additional parton emissions, and LO accuracy for up to two additional parton emissions. The triboson samples only include the fully leptonic decays of the vector bosons. Therefore, there is no overlap between the background triboson and the signal EWK $qqZZjj$ samples. The $t\bar{t}Z$ processes are modeled by SHERPA2.2.0 generator at LO accuracy with up to one additional parton emission using the MEPS@LO set-up [41]. The same algorithms for parton showering, matching, and merging are used as in the QCD $qqZZ$ sample generation. The MC simulation of the triboson and $t\bar{t}Z$ samples are subtracted directly from the data. Table 11 summarizes the details of these samples.

12.2.3 Samples for Fake Background

In addition to the triboson and $t\bar{t}$Z samples, there are additional backgrounds in the analysis coming from events with one or more non-prompt or fake leptons. These fake backgrounds

Process	Description	Generator	PDF	Accuracy
$pp \to W^{(*)}W^{(*)}Z^{(*)} \to 4\ell2\nu$		SHERPA2.2.2		
$pp \to W^{(*)}Z^{(*)}Z^{(*)} \to 5\ell1\nu$	inclusive	SHERPA2.2.2	NNPDF3.0NNLO	$0,1j@NLO + 2j@LO$
$pp \to Z^{(*)}Z^{(*)}Z^{(*)} \to 6\ell$		SHERPA2.2.2		
$pp \to t\bar{t} + Z(\to 2\ell)$	$m_{ll} > 5$ GeV	SHERPA2.2.0	NNPDF3.0NNLO	LO

Table 11: List of background MC samples used in the analysis. Each process consists of three different generation campaigns corresponding to the data-taking conditions of the ATLAS Run2 data-taking periods.

are estimated using a data-driven method discussed in detail in Section 14.1. A set of MC samples are used to develop and validate the data-driven fake background estimation procedure. There are three sources of events that could contribute as a source for fake background events. The first type of events is from a Z-boson production in association with jets $pp \to Z^{(*)} \to 2\ell + jets$, which is simulated for both three or more leptons using SHERPA2.2.1. The subdominant process is events from $t\bar{t} \to 2\ell$ production in which both top quarks decay semileptonically which is simulated with POWHEG+PYTHIA8 and uses the A14NNPDF23LO PDF set [42]. The third type of fake backgrounds arises from the WZ production in which both bosons decay leptonically $pp \to WZ \to 2\ell1\nu$ and is simulated using SHERPA2.2.2. Table 12 summarizes the different processes and MC generators used to estimate the fake background.

Process	Description	Generator	PDF	Accuracy
$pp \to Z^{(*)} \to 2e + jets$				
$pp \to Z^{(*)} \to 2\mu + jets$	inclusive	SHERPA2.2.2	NNPDF3.0NNLO	$NLO + 2j, LO + 4j$
$pp \to Z^{(*)} \to 2\tau + jets$				
$pp \to t\bar{t} \to 2\ell$	inclusive	POWHEG+PYTHIA8	A14NNPDF23LO	LO
$pp \to WZ \to 2\ell1\nu$	inclusive	SHERPA2.2.2	NNPDF3.0NNLO	$NLO + 1j, LO + 3j$

Table 12: List of MC samples used in the estimation and validation of the data-driven fake background estimation.
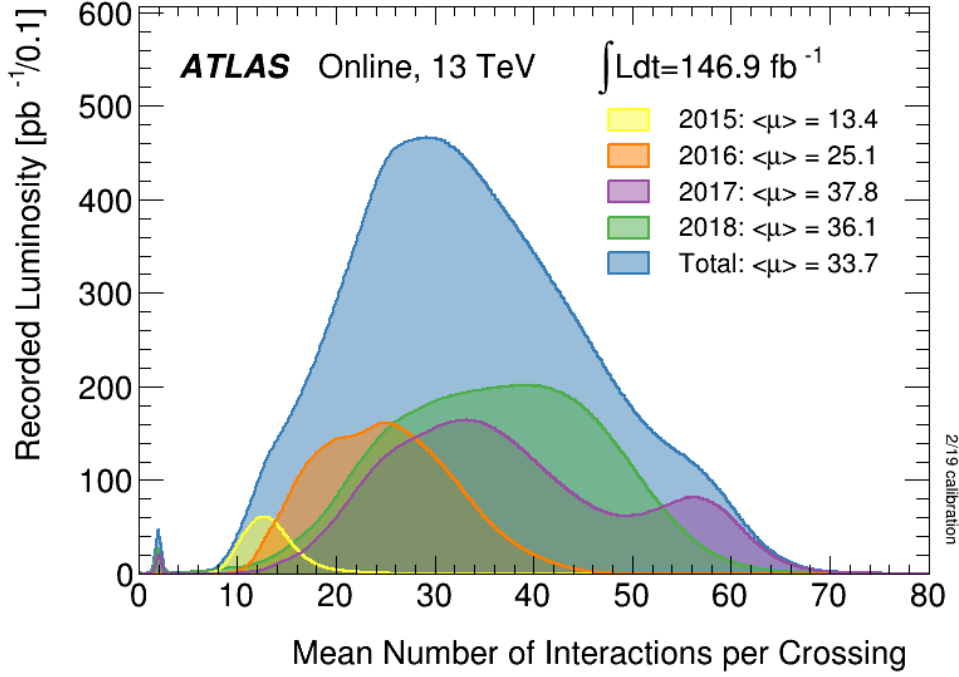
Figure 10: Pile-up distributions in different Run-2 data-taking period. [32]

12.3   Event Weights

The raw predictions from the MC generators are completely unscaled and cannot be compared to the data from the detector directly. Each event generated by the MC needs to be scaled based on the cross-section of a given process normalized to the total sum of all the weights from events generated and multiplied by the integrated luminosity of the data-taking period. As shown by figure 10, the pileup distribution is different for the different data-taking periods. The MC-generated events are modified to correctly simulate the effect of pileup distribution imitating that of the data. Additionally, a set of measurement-related corrections are included in the event weight. These corrections named scaled factors (SF) correct the reconstruction, identification, isolation, and trigger efficiencies in the MC to match that of measured data. The total event weight for MC generated event is a product of the normalized generator weight scaled to match the pile-up profile and all scale factors.

13 Definition of Measured Observables

The primary results of the thesis are differential cross-sections of following 11 different kinematic observables:

- $m_{4\ell}$: invariant mass of the four-leptons (or 2 Z-bosons)

- m_{jj}: invariant mass of the dijet

- $p_{T,4\ell}$: transverse momentum of the four-leptons

- $p_{T,jj}$: transverse momentum of the dijet

- $p_{T,4\ell jj}$: transverse momentum of the four-leptons and the dijet

- $s_{T,4\ell jj}$: scalar transverse momentum of the four-leptons and the dijet

- $\Delta\phi_{jj}^{signed}$: difference in the azimuthal angle between the two jets in the dijet, ordered according to their rapidity,i.e.

$$\Delta\phi_{jj}^{signed} = \begin{cases} \phi(j_1) - \phi(j_2) & \text{if } y_{j_1} > y_{j_2} \\ \phi(j_2) - \phi(j_1) & \text{otherwise} \end{cases}$$

- Δy_{jj}: absolute value of rapidity difference between the leading and the sub-leading jets in the dijet

- ζ: centrality of the system

- $cos\theta_{\ell 1 \ell 2}^*$: cosine of the decay angle of the negative lepton of the leading pair in the pair's rest frame as shown by figure 11

- $cos\theta_{\ell 3 \ell 4}^*$: cosine of the decay angle of the negative lepton of the sub-leading pair in the pair's rest frame as shown by figure 11
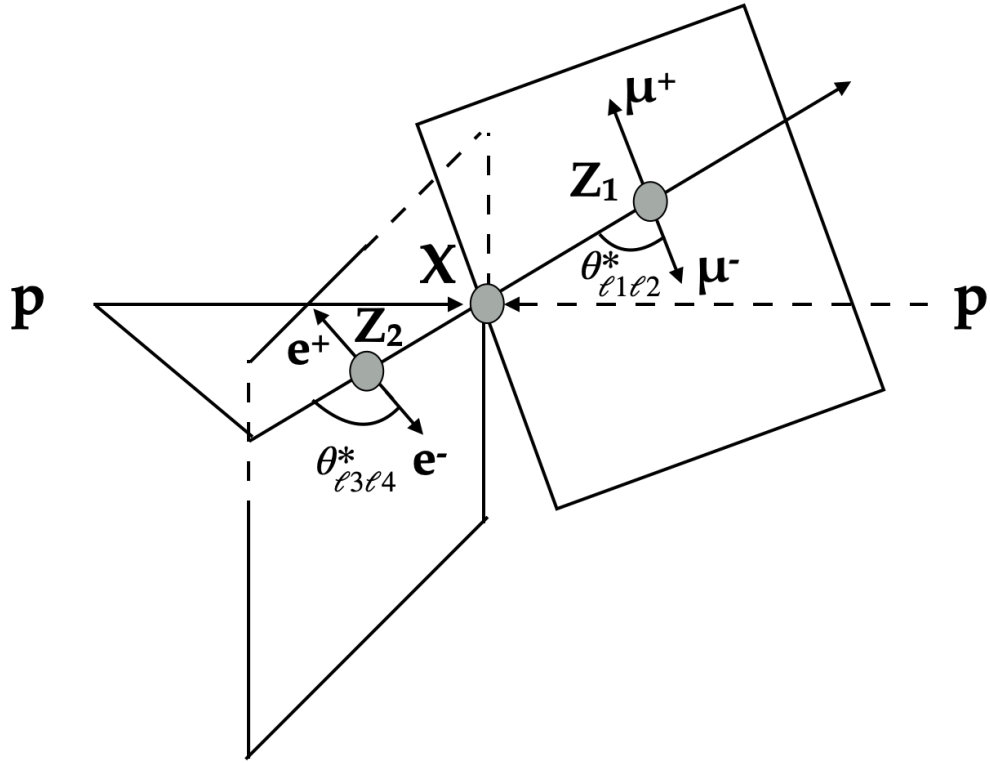
43

Figure 11: Figure showing the decay angle $\theta^*_{\ell1\ell2}$ ($\theta^*_{\ell3\ell4}$) of the negative lepton in the primary (secondary) pair's rest frame. [6].

Chapter V: Analysis Strategy

14 Background

14.1 Data Driven Estimate of Fake Background

14.1.1 Lepton Composition

14.1.2 Control Regions

14.1.3 Fake Efficiency

14.1.4 Method Validation

14.1.5 Signal Region Estimation

15 Unfolding

16 Uncertainties on the Measurement

Chapter VI: Results

17   Differential Cross-sections

18   Effective Field Theory ReInterpretation

Chapter VII: Conclusion

Chapter VIII: **Outlook**

19 Run-3

20 High Luminosity LHC

References

[1] P.A. Zyla et al. Review of Particle Physics. *PTEP*, 2020(8):083C01, 2020.

[2] Francis Halzen and Alan Martin. *Quarks & Leptons: An introductory course in modern particle physics*. John Wiley & Sons, New York, USA, 1984.

[3] Wikipedia contributors. Standard Model of Elementary Particles. https://en.wikipedia.org/wiki/Standard_Model, 2019. [Online; accessed 05-November-2022].

[4] A. D. Martin, W. J. Stirling, R. S. Thorne, and G. Watt. Parton distributions for the LHC. *Eur. Phys. J. C*, 63:189–285, 2009.

[5] The ATLAS Collaboration. Luminosity determination in pp collisions at $\sqrt{s} = 13$ TeV using the ATLAS detector at the LHC. Technical report, CERN, 6 2019.

[6] Yanyan Gao and Andrei V. Gritsan and Zijin Guo and Kirill Melnikov and Markus Schulze and Nhan V. Tran. Spin determination of single-produced resonances at hadron colliders. *Physical Review D*, 81(7), apr 2010.

[7] Mark Thomson. *Modern particle physics*. Cambridge University Press, New York, 2013.

[8] E. Noether. Invariante variationsprobleme. *Nachrichten von der Gesellschaft der Wissenschaften zu Göttingen, Mathematisch-Physikalische Klasse*, 1918:235–257, 1918.

[9] Bernabeu, Jose", and Murillo, Jesús Carnicer and Michelini, Marisa and Perea, Carmen. *Fundamental Physics and Physics Education Research*, chapter Symmetries in the Standard Model, pages 3–16. Springer International Publishing, Cham, 2021.

[10] Sheldon L. Glashow. Partial-symmetries of weak interactions. *Nuclear Physics*, 22(4):579–588, 1961.

[11] C. N. Yang and R. L. Mills. Conservation of Isotopic Spin and Isotopic Gauge Invariance. *Phys. Rev.*, 96:191–195, Oct 1954.

[12] Nguyen, K. The Higgs Mechanism, 2009.

[13] M. E. Peskin , D. V. Schroeder. *An Introduction to Quantum Field Theory*. Westview PRESS, Colorado, USA, 1995.

[14] Buchmüller, W. and Lüdeling, C. Field Theory and Standard Model, 2006.

[15] CMS Collaboration. Observation of a new boson at a mass of 125 GeV with the CMS experiment at the LHC. *Physics Letters B*, 716(1):30–61, sep 2012.

[16] The ATLAS Collaboration. Observation of a new particle in the search for the Standard Model Higgs boson with the ATLAS detector at the LHC. *Physics Letters B*, 716(1):1–29, 2012.

[17] The CDF II Collaboration. High-precision measurement of the W boson mass with the CDF II detector. *Science*, 376(6589):170–176, 2022.

[18] Richard Massey, Thomas Kitching, and Johan Richard. The dark matter of gravitational lensing. *Reports on Progress in Physics*, 73(8):086901, jul 2010.

[19] Peter Skands. QCD for Collider Physics, 2011.

[20] Sergey Alekhin, Kirill Melnikov, and Frank Petriello. Fixed target Drell-Yan data and NNLO QCD fits of parton distribution functions. *Phys. Rev. D*, 74:054033, Sep 2006.

[21] Sergey et al. Alekhin. The PDF4LHC Working Group Interim Report, 2011.

[22] Andy Buckley et al. General-purpose event generators for LHC physics. *Physics Reports*, 504(5):145–233, 2011.

[23] The CMS Collaboration. Evidence for electroweak production of four charged leptons and two jets in proton-proton collisions at s=13TeV. *Physics Letters B*, 812:135992, 2021.

[24] Jager, B., Karlberg, A. and Zanderighi, G. . Electroweak ZZjj production in the Standard Model and beyond in the POWHEG-BOX V2. *J. High Energ. Phys.*, 141, 2014.

[25] A. Denner and T. Hahn. Radiative corrections to W+W- → W+W- in the electroweak standard model. *Nuclear Physics B*, 525(1-2):27–50, 1998.

[26] Tao Han and David Krohn and Lian-Tao Wang and Wenhan Zhu. New physics signals in longitudinal gauge boson scattering at the LHC. *J. High Energ. Phys.*, 2010(3), mar 2010.

[27] Eduardo da Silva Almeida and O. J. P. Éboli and M. C. Gonzalez–Garcia. Unitarity constraints on anomalous quartic couplings. *Physical Review D*, 101(11), jun 2020.

[28] Jung Chang, Kingman Cheung, Chih-Ting Lu, and Tzu-Chiang Yuan. WW Scattering in the Era of Post Higgs Discovery. *Physical Review D*, 87(9), may 2013.

[29] ATLAS Collaboration. Observation of electroweak production of two jets and a *Z*-boson pair, 2020.

[30] Khoze, V., Ryskin, M., Stirling, W. et al. A Z-monitor to calibrate Higgs production via vector boson fusion with rapidity gaps at the LHC. *Eur. Phys. J.*, C 26:429–440, 2003.

[31] G. Avoni et al. The new LUCID-2 detector for luminosity measurement and monitoring in ATLAS. *Journal of Instrumentation*, 13(07):P07017, jul 2018.

[32] The ATLAS Collaboration. ATLAS data quality operations and performance for 2015-2018 data-taking. *Journal of Instrumentation*, 15(04):P04003–P04003, apr 2020.

[33] S. Agostinelli et al. GEANT4–a simulation toolkit. *Nucl. Instrum. Meth. A*, 506:250–303, 2003.

[34] Enrico Bothmann, Gurpreet Singh Chahal, Stefan Höche, Johannes Krause, Frank Krauss, Silvan Kuttimalai, Sebastian Liebschner, Davide Napoletano, Marek Schönherr, Holger Schulz, Steffen Schumann, and Frank Siegert. Event generation with Sherpa 2.2. *SciPost Physics*, 7(3), sep 2019.

[35] Richard D. Ball, , Valerio Bertone, Stefano Carrazza, Christopher S. Deans, Luigi Del Debbio, Stefano Forte, Alberto Guffanti, Nathan P. Hartland, José I. Latorre, Juan Rojo, and Maria Ubiali. Parton distributions for the LHC run II. *Journal of High Energy Physics*, 2015(4), apr 2015.

[36] S. Schumann and F. Krauss. A parton shower algorithm based on catani-seymour dipole factorisation. *Journal of High Energy Physics*, 2008(03):038, mar 2008.

[37] Höche, S., Krauss, F., Schönherr, M. et al. QCD matrix elements + parton showers. The NLO case. *J. High Energ. Phys.*, 2013(27), 2013.

[38] J. Alwall and R. Frederix and S. Frixione and V. Hirschi and F. Maltoni and O. Mattelaer and H.-S. Shao and T. Stelzer and P. Torrielli and M. Zaro. The automated computation of tree-level and next-to-leading order differential cross sections, and their matching to parton shower simulations. *Journal of High Energy Physics*, 2014(7), jul 2014.

[39] Torbjörn Sjöstrand and Stephen Mrenna and Peter Skands. A brief introduction to PYTHIA 8.1. *Computer Physics Communications*, 178(11):852–867, jun 2008.

[40] Barbara Jäger and Alexander Karlberg and Giulia Zanderighi. Electroweak ZZjj production in the Standard Model and beyond in the POWHEG-BOX V2. *Journal of High Energy Physics*, 2014(3), mar 2014.

[41] Stefano Catani and Frank Krauss and Bryan R Webber and Ralf Kuhn. Qcd matrix elements + parton showers. *Journal of High Energy Physics*, 2001(11):063–063, nov 2001.

[42] Torbjorn Sjostrand, Stephen Mrenna, and Peter Z. Skands. A Brief Introduction to PYTHIA 8.1. *Comput. Phys. Commun.*, 178:852–867, 2008.

Appendices